Metal telluride nanosheets by scalable solid lithiation and exfoliation

https://doi.org/10.1038/s41586-024-07209-2

Received: 21 April 2023

Accepted: 20 February 2024

Liangzhu Zhang[1,2,3,10], Zixuan Yang[4,10], Shun Feng[5], Zhuobin Guo[1,6], Qingchao Jia[2,3], Huidan Zeng[2,3], Yajun Ding[1], Pratteek Das[1], Zhihong Bi[1,6], Jiaxin Ma[1], Yunqi Fu[4], Sen Wang[1], Jinxing Mi[1], Shuanghao Zheng[1,7], Mingrun Li[1], Dong-Ming Sun[5], Ning Kang[4]✉, Zhong-Shuai Wu[1,7]✉ & Hui-Ming Cheng[5,8,9]✉

Transition metal tellurides (TMTs) have been ideal materials for exploring exotic properties in condensed-matter physics, chemistry and materials science[1–3]. Although TMT nanosheets have been produced by top-down exfoliation, their scale is below the gram level and requires a long processing time, restricting their effective application from laboratory to market[4–8]. We report the fast and scalable synthesis of a wide variety of MTe_2 (M = Nb, Mo, W, Ta, Ti) nanosheets by the solid lithiation of bulk MTe_2 within 10 min and their subsequent hydrolysis within seconds. Using $NbTe_2$ as a representative, we produced more than a hundred grams (108 g) of $NbTe_2$ nanosheets with 3.2 nm mean thickness, 6.2 μm mean lateral size and a high yield (>80%). Several interesting quantum phenomena, such as quantum oscillations and giant magnetoresistance, were observed that are generally restricted to highly crystalline MTe_2 nanosheets. The TMT nanosheets also perform well as electrocatalysts for lithium–oxygen batteries and electrodes for microsupercapacitors (MSCs). Moreover, this synthesis method is efficient for preparing alloyed telluride, selenide and sulfide nanosheets. Our work opens new opportunities for the universal and scalable synthesis of TMT nanosheets for exploring new quantum phenomena, potential applications and commercialization.

TMTs have been investigated less thoroughly than other 2D materials despite being some of the most fascinating materials for both fundamental research and industrial applications[9–11]. Several TMTs, such as WTe_2 and $MoTe_2$, have been recently investigated for a variety of quantum phenomena, including an extremely large magnetoresistance, topologically nontrivial phases and coupled ferroelectricity and superconductivity[12–14]. 2H–$MoTe_2$ nanosheets have great potential as electrocatalysts for the efficient production of H_2O_2 and green H_2 (refs. 15,16). To promote the use of TMT nanosheets from a laboratory to an industrial scale, safe, reproducible and scalable synthesis techniques must be developed[4,5].

Exfoliation techniques, such as ball milling, liquid-phase exfoliation, along with intercalation-based exfoliation, have been used as ‘top-down’ methods for mass producing nanosheets from their bulk counterparts[6–8,17–22]. Ball milling and liquid exfoliation are not easily scalable because they produce nanosheets with a sub-micrometre lateral size and poor repeatability[7,17]. Intercalation-based exfoliation, on the other hand, by intercalating guest ions or molecules between the layers of bulk crystals driven by electrochemical or chemical methods and delaminating the crystals into large few-layer and monolayer nanosheets with solution processability and a low energy cost, is a more promising approach for producing high-quality TMT nanosheets[19]. However, electrochemical intercalation-based exfoliation requires the use of a single-crystal electrode or coating powders on a conductive substrate, limiting the production scale and requiring cumbersome steps[6,18,21]. Chemical intercalation-based exfoliation has potential for the scalable production of nanosheets from their bulk powders. Unfortunately, commonly used organolithium as an intercalation reagent is highly explosive in ambient atmosphere, requires strictly controlled laboratory conditions and is difficult to intercalate into TMT crystals because of their strong interlayer binding energy[22–24]. At present, the production of TMT nanosheets remains below the gram scale and requires a long processing time of more than 30 min using existing exfoliation methods. Compared with solvent chemical intercalation-based exfoliation, solid-state intercalation has great advantages in safety and scalability[25]. Tetrahydroborates are promising reducing agents and are stable enough to be handled in air for a short duration[26]. Therefore, they can be exploited for the solid lithiation and exfoliation of a large quantity of TMTs into high-quality TMT nanosheets.

---

[1]State Key Laboratory of Catalysis, Dalian Institute of Chemical Physics, Chinese Academy of Sciences, Dalian, China. [2]School of Materials Science and Engineering, East China University of Science and Technology, Shanghai, China. [3]Shanghai Electronic Chemicals innovation Institute, East China University of science and Technology, Shanghai, China. [4]Key Laboratory for the Physics and Chemistry of Nanodevices and Center for Carbon-based Electronics, School of Electronics, Peking University, Beijing, China. [5]Shenyang National Laboratory for Materials Science, Institute of Metal Research, Chinese Academy of Sciences, Shenyang, China. [6]University of Chinese Academy of Sciences, Beijing, China. [7]Dalian National Laboratory for Clean Energy, Chinese Academy of Sciences, Dalian, China. [8]Shenzhen Key Laboratory of Energy Materials for Carbon Neutrality, Shenzhen Institute of Advanced Technology, Chinese Academy of Sciences, Shenzhen, China. [9]Faculty of Materials Science and Energy Engineering, Shenzhen University of Advanced Technology, Shenzhen, China. [10]These authors contributed equally: Liangzhu Zhang, Zixuan Yang. ✉e-mail: nkang@pku.edu.cn; wuzs@dicp.ac.cn; hm.cheng@siat.ac.cn

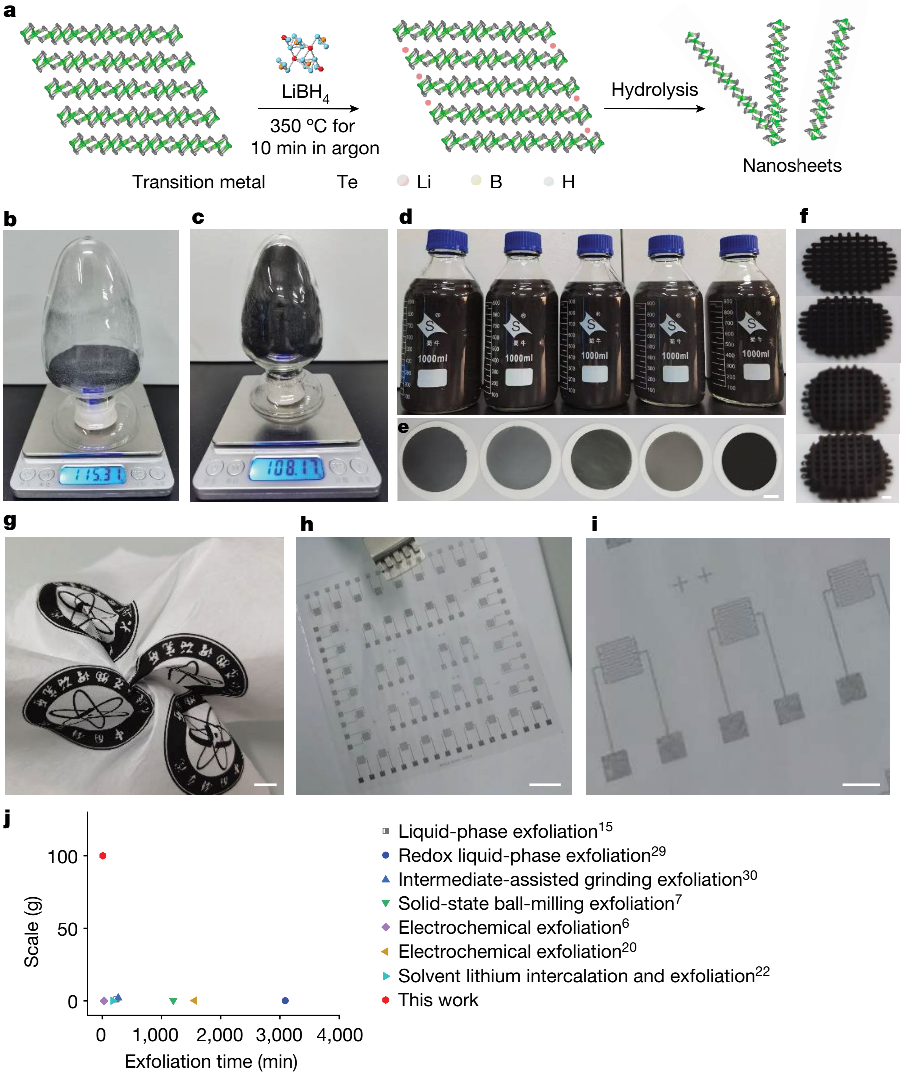

Fig. 1 | Synthesis of 2D TMT nanosheets and the applications of TMT inks. **a**, Illustration of the solid lithiation and exfoliation of TMT nanosheets. **b**,**c**, Photographs of bulk $NbTe_2$ crystals (**b**) and $NbTe_2$ nanosheets (**c**). **d**, Photograph of $NbTe_2$ water dispersions in 1-L bottles with a concentration of 1 mg mL^{-1}. **e**, Photographs of $MoTe_2$, WTe_2, $NbTe_2$, $TaTe_2$ and $TiTe_2$ films (from left to right) with a diameter of 47 mm. Scale bar, 10 mm. **f**, 3D-printed scaffold with a microlattice pattern created using $NbTe_2$ nanosheet ink. Scale bar, 1 mm. **g**, Distorted and folded white non-woven fabric with a screen-printed DICP logo using $NbTe_2$ nanosheet ink. Scale bar, 10 mm. **h**, Array of $NbTe_2$-based interdigital microelectrodes on glass, fabricated by photolithography. Scale bar, 10 mm. **i**, Enlarged view of **h**. Scale bar, 2 mm. **j**, Exfoliation time versus production scale of TMT nanosheets prepared by different methods, including liquid-phase exfoliation, electrochemical exfoliation, grinding exfoliation, ball-milling exfoliation, solvent lithium intercalation and exfoliation, and solid lithiation and exfoliation. Superscript numbers are references.

We report an ultrafast, repeatable and hundred-gram-scale production method to synthesize $MoTe_2$, WTe_2, $NbTe_2$, $TaTe_2$ and $TiTe_2$ nanosheets by solid lithiation and exfoliation. The synthesis of TMT nanosheets using lithium intercalation and hydrolysis is illustrated in Fig. 1a. First, bulk TMT crystals were prepared by chemical vapour transport (CVT) (Supplementary Fig. 1). A mixture of bulk TMT crystals and $LiBH_4$ was then heated at 350 °C for 10 min in an argon atmosphere to complete the solid-state lithium intercalation, which is much faster than the solvothermal process (3 h)[22]. X-ray diffraction (XRD) patterns of the lithiated intermediate of Li_xMTe_2 (x is the molar ratio of $LiBH_4$ to MTe_2 in the prepared mixture) showed that the new (002)* peak shifted to a lower angle compared to the bulk MTe_2 crystal, indicating an increased interlayer spacing caused by lithium-ion intercalation[27] (Supplementary Fig. 2). The lithiated material was then exfoliated into nanosheets by hydrolysis. Taking $NbTe_2$ as an example, lithiated $NbTe_2$ powder was hydrolysed into $NbTe_2$ nanosheets by adding distilled water, resulting in the formation of a black colloidal suspension within seconds, which exhibits the Tyndall effect (Extended Data Fig. 1). This method is general and can be used for producing a wide range of TMT nanosheets, including $MoTe_2$, WTe_2, $NbTe_2$, $TaTe_2$ and $TiTe_2$.

To optimize the exfoliation process, the optimum molar ratio of $LiBH_4$ to TMT bulk crystals and the time of lithium intercalation were investigated. In general, TMT crystals were found to be unstable when the duration of lithium intercalation was long. For $MoTe_2$, WTe_2, $NbTe_2$, $TaTe_2$ and $TiTe_2$, the decomposition of the nanosheets became more severe as the lithium intercalation time was increased from 1 to 6 h (Supplementary Fig. 3). The decomposition products were Te nanobelts (Extended Data Fig. 2), which may be formed in two steps according to the following equations[28]: (1) $MTe_2 + LiBH_4 \rightarrow Li_2Te + M + B + H_2$ and (2) $Li_2Te + H_2O \rightarrow Te + H_2 + LiOH$. The nanobelts were found on VTe_2 and $ZrTe_2$ nanosheets after only 10 min of intercalation (Supplementary Figs. 4 and 5). The exfoliation yield increased with the molar ratio (x) of $LiBH_4$ to TMT bulk crystals from 0.1 to 0.75 (Extended Data Fig. 3). It was found that x ranging from 0.75 to 1 was

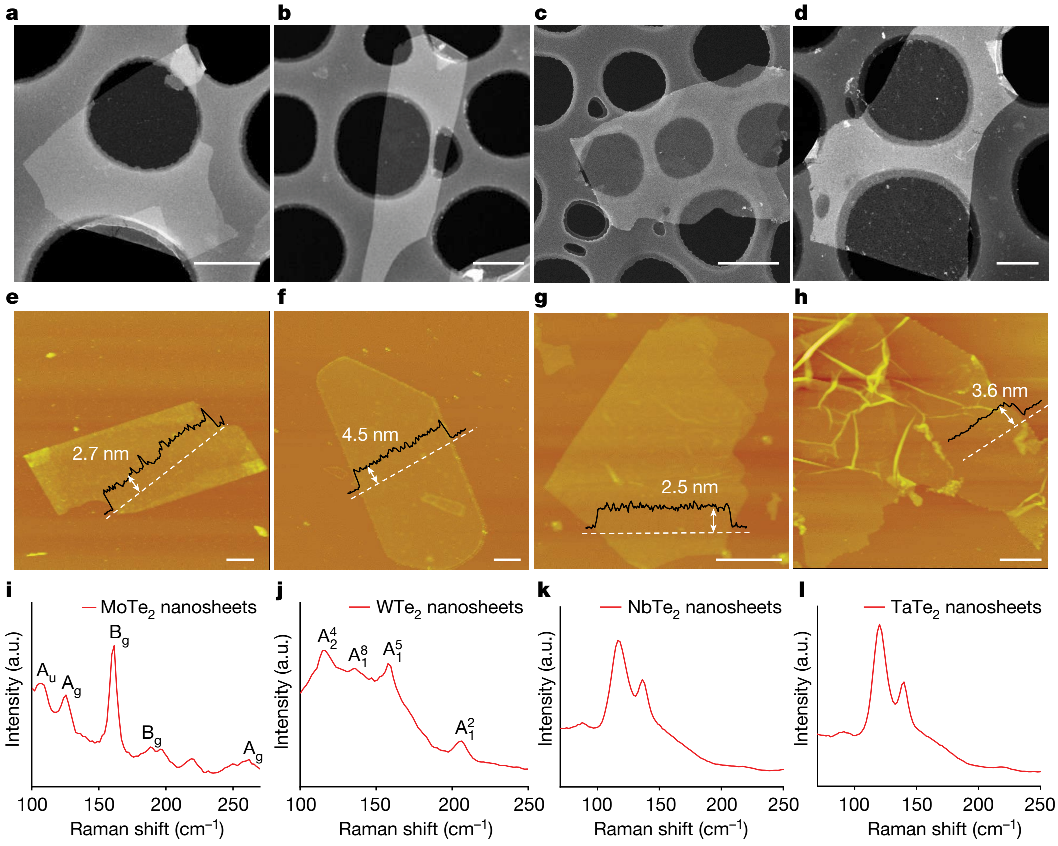

Fig. 2 | Morphology and Raman characterizations of TMT nanosheets. a–d, SEM images. Scale bars, 1 μm. **e–h**, AFM images. Scale bars, 0.5 μm. **i–l**, Raman spectra. MoTe$_2$, WTe$_2$, NbTe$_2$ and TaTe$_2$ nanosheets shown from left to right. a.u., arbitrary units.

suitable for achieving high exfoliation yields of more than 60% for MoTe$_2$, 50% for WTe$_2$, 80% for NbTe$_2$, 80% for WTe$_2$ and 40% for TiTe$_2$. Using NbTe$_2$ as an example, we demonstrated the scaled-up production of 108 g of NbTe$_2$ nanosheet powder (Fig. 1b,c) and was readily dispersible in an aqueous medium with a concentration of 1 mg mL^{-1} (Fig. 1d). Films of MoTe$_2$, WTe$_2$, NbTe$_2$, TaTe$_2$ and TiTe$_2$ nanosheets were easily prepared from the corresponding colloidal dispersions by vacuum filtration (Fig. 1e). The NbTe$_2$ nanosheet powder could also be readily processed into various inks. Scaffolds with microlattice patterns, a DICP (Dalian Institute of Chemical Physics) logo on flexible non-woven fabric and paper and high-resolution interdigital microelectrodes were fabricated by 3D printing, screen printing and photolithography, respectively, paving the way for versatile applications (Fig. 1f–i and Supplementary Fig. 6). Figure 1j shows comparisons of the efficiency and scalability of solid lithiation and exfoliation for producing TMT nanosheets with other exfoliation methods, such as liquid-phase exfoliation, intermediate-assisted grinding exfoliation, solid-state ball-milling exfoliation, electrochemical molecular intercalation and exfoliation, and solvent lithium intercalation and exfoliation[6,7,15,20,22,29,30] (Supplementary Table 1). Our method has the shortest processing time of 10 min and the best scalability (hundred-gram range) among all methods. To the best of our knowledge, our exfoliation method is the only one that allows production on such a large scale in only 10 min.

The morphology and size distribution of the 2D TMT nanosheets were examined by scanning electron microscopy (SEM) (Fig. 2a–d and Supplementary Fig. 7). All of the TMT nanosheets were found to be thin with a micrometre-scale lateral size. From statistical analysis (Supplementary Fig. 8), the mean lateral size of the nanosheets was measured to be 3.5 μm for MoTe$_2$, 2.9 μm for WTe$_2$, 6.2 μm for NbTe$_2$, 3.1 μm for TaTe$_2$ and 1.6 μm for TiTe$_2$. These values are much larger than the sub-micrometre lateral sizes of TMT nanosheets prepared by liquid-phase or solid-state ball-milling exfoliation[7,17]. Atomic force microscopy (AFM) images show that the as-prepared TMT nanosheets are thin and have a flat morphology. MoTe$_2$, WTe$_2$, NbTe$_2$, TaTe$_2$ and TiTe$_2$ nanosheets have average thicknesses of 5.8, 4.9, 3.2, 5.0 and 9.8 nm, respectively (Fig. 2e–h and Supplementary Figs. 9 and 10). Notably, the exfoliation yield (40–80%) and large lateral size (>2 μm) with a narrow thickness distribution (1–14 nm) are also competitive with other exfoliation methods (Supplementary Table 1). The Raman spectra of TMT nanosheets are consistent with those in previous reports[10,31–33] (Fig. 2i–l and Supplementary Fig. 11).

X-ray photoelectron spectroscopy (XPS) differentiates the surface bonding features of the TMT nanosheets from those of the corresponding bulk crystals. High-resolution XPS spectra of Mo 3d, W 4f, Nb 3d, Ta 4f, Ti 2p and Te 3d are given in Supplementary Figs. 12–16. Large integrated areas are observed under the Te–O peak around 576.1 eV and the Te 3d peak around 586.4 eV for all of the nanosheets, indicating surface oxidation, which is consistent with what is seen in liquid-exfoliated TMT nanosheets[34,35] (Supplementary Figs. 12–16). Furthermore, elemental analysis by energy-dispersive spectrometry (EDS) shows that the molar ratios of tellurium to the metal in MoTe$_2$ and NbTe$_2$ are 1.94 and 1.85, respectively, which are close to the expected stoichiometric ratio of 2. However, WTe$_2$, TaTe$_2$ and TiTe$_2$ nanosheets have non-stoichiometric molar ratios of 2.53, 2.42 and 2.39, respectively, possibly caused by Te-rich clusters on the surface of the nanosheets that may contribute a larger amount of elemental Te (Supplementary Figs. 17 and 18).

The crystal structures and crystallinity of the TMT nanosheets were characterized by transmission electron microscopy (TEM). A quasi-1D structure of zigzag chains in MoTe$_2$ and WTe$_2$ nanosheets

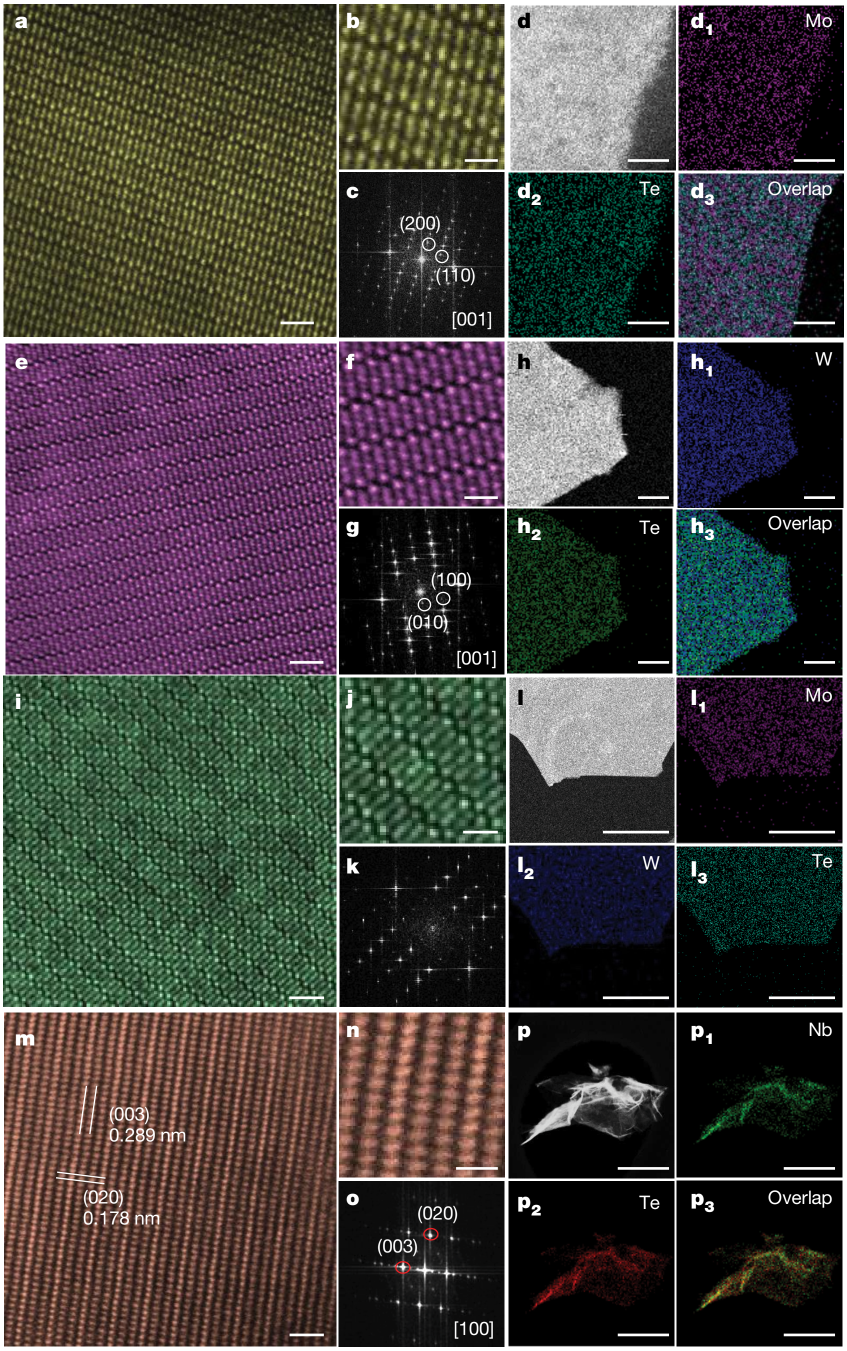

Fig. 3 | Structural characterizations of $MoTe_2$, WTe_2, $Mo_{0.5}W_{0.5}Te_2$ and $NbTe_2$ nanosheets. **a**,**e**,**i**,**m**, Atomic-resolution HAADF-STEM images. Scale bars, 1 nm. **b**,**f**,**j**,**n**, Magnified HAADF-STEM images. Scale bars, 0.5 nm. **c**,**g**,**k**,**o**, Corresponding FFT patterns of $MoTe_2$, WTe_2, $Mo_{0.5}W_{0.5}Te_2$ and $NbTe_2$, respectively. **d**, HAADF-STEM image and EDS elemental maps (**d_1**–**d_3**) of Mo, Te and mixed Mo and Te, respectively. Scale bars, 5 nm. **h**, HAADF-STEM image and EDS elemental maps (**h_1**–**h_3**) of W, Te and mixed W and Te, respectively. Scale bars, 100 nm. **l**, HAADF-STEM image and EDS elemental maps (**l_1**–**l_3**) of Mo, W and Te, respectively. Scale bars, 1 µm. **p**, HAADF-STEM image and EDS elemental maps (**p_1**–**p_3**) of Nb, Te and mixed Nb and Te, respectively. Scale bars, 0.5 µm.

was observed in atomic high-angle annular dark-field scanning TEM (HAADF-STEM) images and the rectangular reciprocal lattices shown in fast Fourier transform (FFT) images confirm the 1T′ and T_d phases and their single-crystal nature[36] (Fig. 3a–c,e–g). Also, a single-crystal phase with a representative zigzag chain atomic structure was observed in a $Mo_{0.5}W_{0.5}Te_2$ nanosheet (Fig. 3i–k). The 1T phase of $NbTe_2$ was verified by atomically resolved STEM and FFT images, showing dominant (003) and (020) planes with a lattice spacing of 0.289 and 0.178 nm, respectively[32] (Fig. 3m–o). Energy-dispersive X-ray spectroscopy maps confirm the uniform distribution of the elements in $MoTe_2$, WTe_2, $Mo_{0.5}W_{0.5}Te_2$ and $NbTe_2$ nanosheets (Fig. 3d–d_3,h–h_3,l–l_3,p–p_3). $TaTe_2$ and $TiTe_2$ nanosheets with a 1T structure were characterized by HAADF-STEM (Supplementary Figs. 19 and 20).

This solid lithiation and exfoliation method can be generalized to prepare many alloyed tellurides, such as $Nb_{0.5}Ta_{0.5}Te_2$, NbSeTe and $Mo(SSeTe)_2$. It is also useful for exfoliating selenide nanosheets (MoSSe, TaSSe, $Mo_{0.5}Nb_{0.5}Se_2$, $(MoNbTa)Se_2$, In_2Se_3, $MoSe_2$, $TaSe_2$) and sulfide nanosheets ($Mo_{0.5}Ta_{0.5}S_2$, $Ta_{0.5}Re_{0.5}S_2$, $(MoWTa)S_2$, $(TiZrHf)S_2$, TaS_2). The detailed characterizations of these exfoliated nanosheets are presented in Extended Data Figs. 4 and 5 and Supplementary Figs. 21–48.

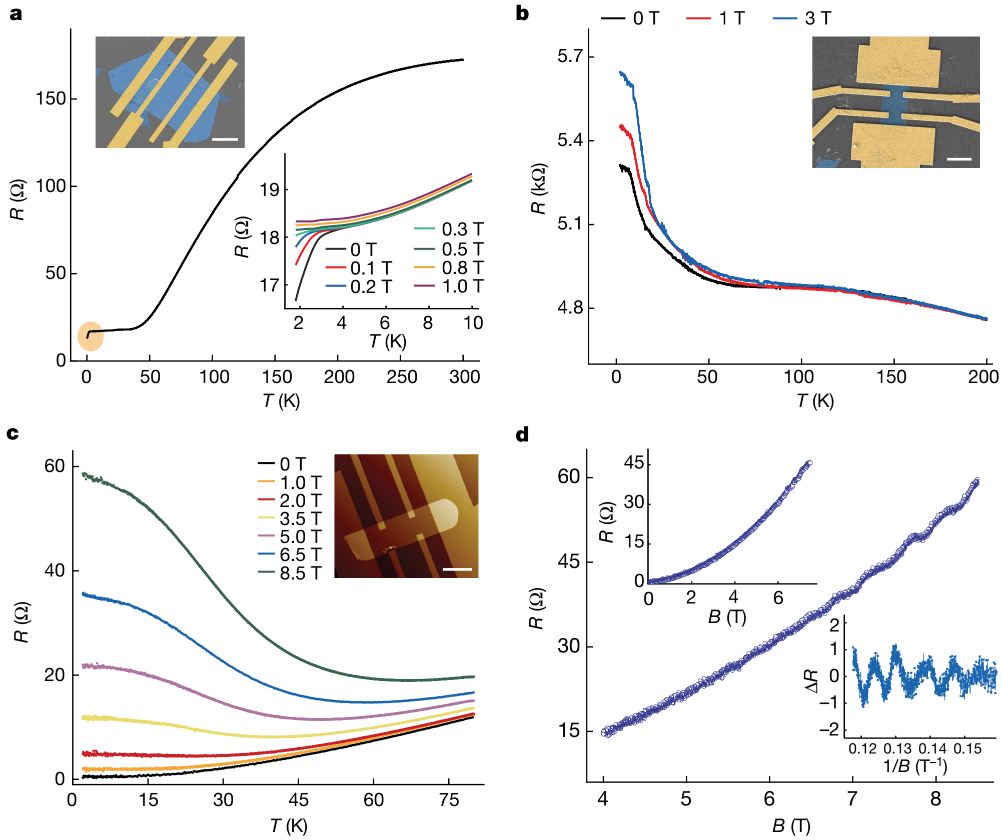

Fig. 4 | Transport properties of exfoliated $MoTe_2$ and WTe_2 nanosheets. **a**, Resistance of 17.2-nm-thick $MoTe_2$ as a function of temperature at zero magnetic field. Upper inset, false-coloured SEM image of a four-terminal device. Scale bar, 5 μm. Lower inset, the resistive transition at temperatures ranging from 1.8 to 10 K in various applied magnetic field strengths. **b**, Temperature-dependent resistance of a 3.1-nm-thick $MoTe_2$ sample under magnetic fields of $B = 0$, 1 and 3 T. Inset, false-coloured SEM image of the Hall-bar device. Scale bar, 2 μm. **c**, Temperature dependence of the resistance of the WTe_2 sample at various magnetic field strengths. Inset, AFM image of a fabricated WTe_2 device. Scale bar, 2 μm. **d**, Magnetoresistance data of a WTe_2 sample in the range 4–8.5 T at $T = 1.8$ K. The resistance oscillations are clearly visible at high fields. Upper inset, magnetoresistance from 0 to 7.5 T at $T = 2$ K, showing a quadratic field dependence with no sign of saturation. Lower inset, quantum oscillations that are periodic in $1/B$.

To characterize the high quality of our 2D TMT nanosheets, $MoTe_2$, WTe_2 and $Mo_{0.5}W_{0.5}Te_2$ were chosen to study their quantum transport properties. A strong thickness-dependent charge-transport behaviour was found in $MoTe_2$ nanosheets. Figure 4a shows the temperature dependence of the resistance for a 17.2-nm-thick $MoTe_2$ nanosheet at zero magnetic field. The R–T curve shows a semimetallic characteristic at high temperature. At low temperature, the resistance is gradually saturated, followed by a drop, suggesting the onset of superconductivity. A magnetic field of about 0.5 T suppresses the overall resistive transition (lower inset in Fig. 4a and Supplementary Fig. 49). An incomplete and broad transition may be related to the inhomogeneity and defects within the nanosheets. $T_{c,onset}$ is about 3 K, which is an order of magnitude larger than that of the bulk $MoTe_2$ (0.25 K) and comparable with that of chemical vapour deposition (CVD)-grown 2D crystals[36,37]. After three months of storage in vacuum, the samples still maintain their metallic features (Supplementary Fig. 50), showing the high device stability of the 2D $MoTe_2$ prepared by this method.

We also found strong thickness-dependent electronic states in $MoTe_2$. Figure 4b shows the temperature dependence of the resistance for a 3.1-nm-thick sample at 0, 1 and 3 T. In contrast to thicker nanosheets, the resistive transition occurs in three stages as the temperature is reduced: at high temperatures (>150 K), the resistance increases slowly and then reaches a plateau from 150 to 50 K. Below about 50 K, a noticeable upturn is seen in $R(T)$, which becomes more pronounced with increasing magnetic field. The resistive transition obtained from another sample with a thickness of 8.4 nm has a non-monotonic temperature dependence, indicating an intermediate transition (Supplementary Fig. 51). These results indicate that a decrease of thickness triggers competition between metallic and insulating behaviours in these lithium intercalation-exfoliated $MoTe_2$ nanosheets. This thickness-dependent magnetotransport behaviour was also found in an exfoliated $Mo_{0.5}W_{0.5}Te_2$ nanosheet (Extended Data Fig. 6). The temperature changes of carrier density (n_c) and Hall mobility (μ_H) show a kink-like feature around 50 K and 150 K (Supplementary Figs. 52 and 53 and Supplementary Table 2), which are the same characteristic temperatures as for the resistive transition. Similar behaviour has been reported previously in a $MoTe_2$ single crystal, which was attributed to the reconstruction of the Fermi surface owing to a thermally driven Lifshitz transition or structural phase transition related to different order topological features[38,39]. Other possibilities are the defect-induced disorder effect, in particular for thin TMT naonsheets[40], or that solid-state intercalation induces a phase domain-wall structure[41]. The carrier density of $MoTe_2$ synthesized using our method is comparable or 1–2 orders of magnitude larger than those of mechanically exfoliated samples, suggesting the charge-carrier doping of the intercalated $MoTe_2$ nanosheets[14,36,42–45] (Supplementary Fig. 54). Further experimental and theoretical studies are needed to understand the influence of the thickness on the phase transitions in 2D TMT nanosheets, and the synthesis strategy reported here may aid that pursuit.

In Fig. 4c, we show the temperature dependence of the resistance of a WTe_2 nanosheet, measured at various magnetic fields. The residual resistivity ratio (ρ_{300K}/ρ_{2K}) at zero magnetic field is around 200, indicating the high crystallinity of the nanosheets. When a perpendicular magnetic field was applied, the R–T curves showed a field-driven

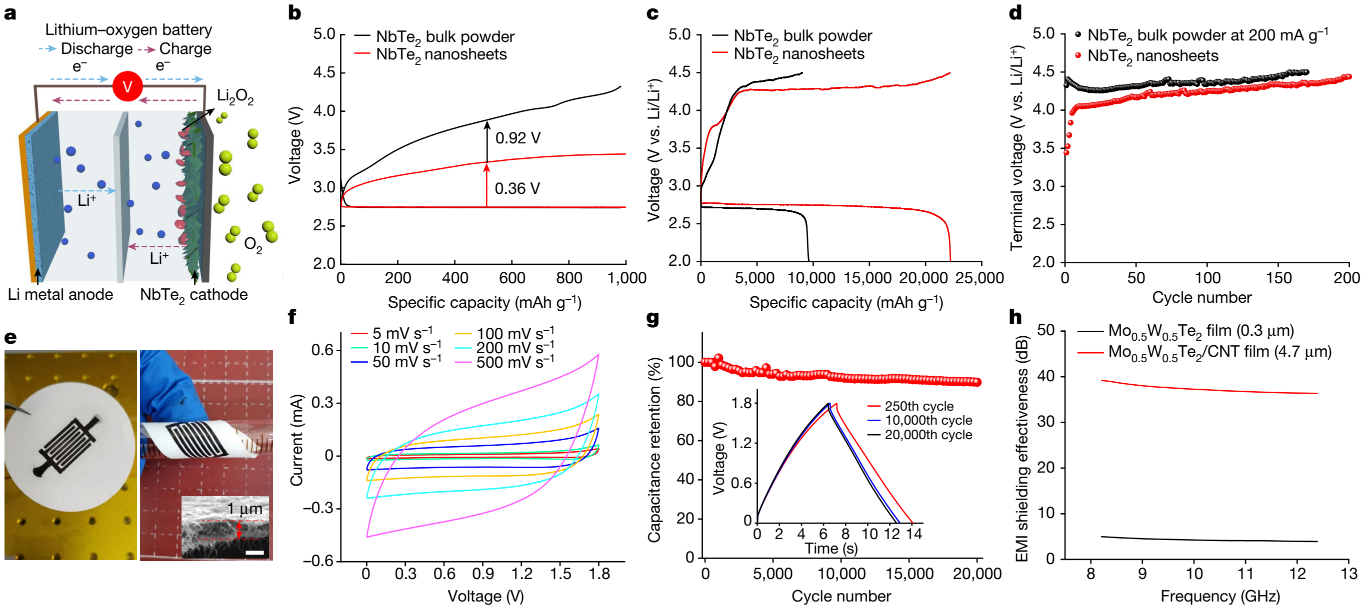

Fig. 5 | Applications of TMT nanosheets produced by solid lithiation and exfoliation. a, Schematic of Li–O_2 batteries. **b**, Discharge–charge profiles of 2D $NbTe_2$ nanosheet and $NbTe_2$ bulk powder cathodes for Li–O_2 batteries under a limited capacity of 1,000 mAh g^{-1} at a current density of 100 mA g^{-1}. **c**, The first discharge–charge profiles of $NbTe_2$ nanosheet and $NbTe_2$ bulk powder cathodes for Li–O_2 batteries obtained at 100 mA g^{-1}. **d**, Terminal discharge voltage versus cycle number of $NbTe_2$ nanosheet- and $NbTe_2$ bulk powder-based Li–O_2 batteries at 200 mA g^{-1}. **e**, Optical image of MSCs fabricated on a cellulose film in the flat (left) and bent (right) states. Inset, cross-sectional SEM image of the $NbTe_2$ film with a thickness of 1 μm. Scale bar, 1 μm. **f**,**g**, Electrochemical performance of 2D $NbTe_2$ nanosheet-based MSCs. **f**, Cyclic voltammetry curves of $NbTe_2$ nanosheet-based MSCs in an electrolyte of $EMIMBF_4$ in acetonitrile ($EMIMBF_4$/ACN). **g**, Long-term cycling stability of $NbTe_2$ nanosheet-based MSCs in an $EMIMBF_4$/ACN electrolyte. Inset, galvanostatic charge/discharge profiles of the 250th, 10,000th and 20,000th cycles. **h**, EMI shielding performance of $Mo_{0.5}W_{0.5}Te_2$ and $Mo_{0.5}W_{0.5}Te_2$/CNT films at the X-band frequency range (8.2–12.4 GHz).

transition from a metallic to insulating-like behaviour. The magnetic field dependence of the resistance at low temperatures has an expected quadratic relationship with no sign of saturation up to 7.5 T (upper inset in Fig. 4d), showing an extremely large positive magnetoresistance. Both phenomena are consistent with previous reports obtained from WTe_2 single bulk crystals, exhibiting Weyl semimetal features[37]. Figure 4d shows the resistance as a function of the magnetic field in the range 4–8.5 T at 1.8 K. For fields larger than 6.4 T, well-resolved resistive oscillations were clearly visible, along with extremely large positive magnetoresistance. After subtracting the smooth background using a second-order polynomial fit, the oscillatory part is plotted as a function of $1/B$ in the lower inset in Fig. 4d. A clear $1/B$ periodic pattern can be observed, which is the characteristic feature of Shubnikov–de Haas (SdH) oscillations. The observation of SdH oscillations indicates the high crystallinity and homogeneity of the WTe_2 nanosheets. From the onset of SdH oscillations, we estimated the transport mobility to be $\mu \approx 1{,}500\ \mathrm{cm^2\,(V\,s)^{-1}}$, comparable with mechanically exfoliated flakes from single crystals and confirming the good electrical performance of our samples for potential applicability in quantum devices.

TMT nanosheets produced by solid lithiation and exfoliation can be applied in catalysis, energy storage and electronics devices, which need a large quantity. As demonstrated, $NbTe_2$ nanosheets were used as robust bifunctional electrocatalysts for reversible Li_2O_2 conversion in high-performance Li–O_2 batteries and has a much lower charge potential of 0.36 V than that of $NbTe_2$ bulk powder (0.92 V), proving their greatly increased catalytic activity (Fig. 5a,b). As a result, an ultrahigh discharge capacity of 22,212 mAh g^{-1}, excellent rate capability and long-term cycling stability of 200 cycles under current densities of 200 and 500 mAh g^{-1} have been achieved for $NbTe_2$ nanosheet-based Li–O_2 batteries, which are much better than those using $NbTe_2$ bulk powder (Fig. 5c,d and Supplementary Figs. 55 and 56). Moreover, $Mo_{0.5}W_{0.5}Te_2$ nanosheets show good lithium storage performance with an initial specific capacity of 510 mAh g^{-1} at 0.3 C and a high rate capacity (152 mAh g^{-1} at 3 C) (Supplementary Fig. 57). Furthermore, $NbTe_2$ nanosheet-based flexible MSCs have areal and volumetric capacitances of 4.8 mF cm^{-2} and 46.5 mF cm^{-3}, respectively, at 5 mV s^{-1} with a large voltage of 1.8 V in an $EMIMBF_4$/ACN electrolyte, as well as an excellent stability with 90% capacitance retention after 20,000 cycles (Fig. 5e–g and Supplementary Fig. 58). Also, a $Mo_{0.5}W_{0.5}Te_2$/carbon nanotube (CNT) film with a well-aligned, compact and nacre-like structure showed an electromagnetic interference (EMI) shielding effectiveness of more than 36.4 dB at 8.2–12.4 GHz with a thickness of only 5 μm, which satisfies common commercial EMI shielding requirements (>20 dB) and has great promise for use in future wearable and portable electronics (Fig. 5h and Supplementary Fig. 59).

In summary, we have developed a general solid lithiation and exfoliation method for the hundred-gram synthesis of high-quality TMT nanosheets that has the potential to revolutionize their commercial manufacture. Owing to their increasing prominence, new layered TMT bulk crystals are expected to be discovered in the future and this method opens the possibility for mass production of their nanosheets. Moreover, these nanosheets have excellent processability to form various inks for fabricating membranes, films, nanocomposites and heterostructures in conjunction with advanced (micro) fabrication techniques, which will accelerate fundamental research and permit their use in many areas of research involving, but not limited to, topological electronics, catalysis, energy storage and flexible electronics.

Online content

Any methods, additional references, Nature Portfolio reporting summaries, source data, extended data, supplementary information, acknowledgements, peer review information; details of author contributions and competing interests; and statements of data and code availability are available at https://doi.org/10.1038/s41586-024-07209-2.

1. Zhou, J. et al. A library of atomically thin metal chalcogenides. *Nature* **556**, 355–359 (2018).
2. Fiori, G. et al. Electronics based on two-dimensional materials. *Nat. Nanotechnol*. **9**, 768–779 (2014).
3. Pomerantseva, E. & Gogotsi, Y. Two-dimensional heterostructures for energy storage. *Nat. Energy* **2**, 17089 (2017).
4. Choi, S. H. et al. Large-scale synthesis of graphene and other 2D materials towards industrialization. *Nat. Commun.* **13**, 1484 (2022).
5. Editorial. Moving towards the market. *Nat. Mater*. **18**, 519. https://doi.org/10.1038/s41563-019-0394-4 (2019).
6. Li, J. et al. Printable two-dimensional superconducting monolayers. *Nat. Mater.* **20**, 181–187 (2021).
7. Zhang, L. et al. Solid phase exfoliation for producing dispersible transition metal dichalcogenides nanosheets. *Adv. Funct. Mater.* **30**, 2004139 (2020).
8. Coleman, J. N. et al. Two-dimensional nanosheets produced by liquid exfoliation of layered materials. *Science* **331**, 568–571 (2011).
9. Li, H. et al. Two-dimensional metal telluride atomic crystals: preparation, physical properties, and applications. *Adv. Funct. Mater.* **31**, 2010901 (2021).
10. Keum, D. H. et al. Bandgap opening in few-layered monoclinic $MoTe_2$. *Nat. Phys*. **11**, 482–486 (2015).
11. Xu, X. et al. Seeded 2D epitaxy of large-area single-crystal films of the van der Waals semiconductor 2H $MoTe_2$. *Science* **372**, 195–200 (2021).
12. Ali, M. N. et al. Large, non-saturating magnetoresistance in WTe_2. *Nature* **514**, 205–208 (2014).
13. Wang, W. et al. Evidence for an edge supercurrent in the Weyl superconductor $MoTe_2$. *Science* **368**, 534–537 (2020).
14. Jindal, A. et al. Coupled ferroelectricity and superconductivity in bilayer T_d-$MoTe_2$. *Nature* **613**, 48–52 (2023).
15. Zhao, X. et al. Selective electrochemical production of hydrogen peroxide at zigzag edges of exfoliated molybdenum telluride nanoflakes. *Natl Sci. Rev.* **7**, 1360–1366 (2020).
16. McGlynn, J. C. et al. The rapid electrochemical activation of $MoTe_2$ for the hydrogen evolution reaction. *Nat. Commun.* **10**, 4916 (2019).
17. Nicolosi, V., Chhowalla, M., Kanatzidis, M. G., Strano, M. S. & Coleman, J. N. Liquid exfoliation of layered materials. *Science* **340**, 1226419 (2013).
18. Yang, S., Zhang, P., Nia, A. S. & Feng, X. Emerging 2D materials produced via electrochemistry. *Adv. Mater.* **32**, 1907857 (2020).
19. Yang, R. et al. Synthesis of atomically thin sheets by the intercalation-based exfoliation of layered materials. *Nat. Synth.* **2**, 101–118 (2023).
20. Yang, R. et al. High-yield production of mono- or few-layer transition metal dichalcogenide nanosheets by an electrochemical lithium ion intercalation-based exfoliation method. *Nat. Protoc.* **17**, 358–377 (2022).
21. Lin, Z. et al. Solution-processable 2D semiconductors for high-performance large-area electronics. *Nature* **562**, 254–258 (2018).
22. Peng, J. et al. High phase purity of large-sized 1T′-MoS_2 monolayers with 2D superconductivity. *Adv. Mater.* **31**, 1900568 (2019).
23. Joensen, P., Frindt, R. F. & Morrison, S. R. Single-layer MoS_2. *Mater. Res. Bull.* **21**, 457–461 (1986).
24. Zheng, J. et al. High yield exfoliation of two-dimensional chalcogenides using sodium naphthalenide. *Nat. Commun.* **5**, 2995 (2014).
25. Tsai, H.-L., Heising, J., Schindler, J. L., Kannewurf, C. R. & Kanatzidis, M. G. Exfoliated-restacked phase of WS_2. *Chem. Mater.* **9**, 879–882 (1997).
26. Kanatzidis, M. G. & Marks, T. J. Tetrahydroborate intercalation reagents. Convenient, straightforward routes to known and new types of layered intercalation compounds. *Inorg. Chem.* **26**, 783–784 (1987).
27. Ono, M. et al. New lithium- and ethylenediamine-intercalated superconductors $Li_x(C_2H_8N_2)_y$ WTe_2. *J. Phys. Soc. Jpn.* **90**, 014706 (2020).
28. Peng, J. et al. Two-dimensional tellurium nanosheets exhibiting an anomalous switchable photoresponse with thickness dependence. *Angew. Chem. Int. Ed.* **57**, 13533–13537 (2018).
29. Jawaid, A. et al. Redox exfoliation of layered transition metal dichalcogenides. *ACS Nano* **11**, 635–646 (2017).
30. Zhang, C. et al. Mass production of 2D materials by intermediate-assisted grinding exfoliation. *Natl Sci. Rev.* **7**, 324–332 (2020).
31. Hangyo, M., Nakashima, S.-I. & Mitsuishi, A. Raman spectroscopic studies of MX_2-type layered compounds. *Ferroelectrics* **52**, 151–159 (1983).
32. Li, J. et al. Synthesis of ultrathin metallic MTe_2 (M = V, Nb, Ta) single-crystalline nanoplates. *Adv. Mater.* **30**, 1801043 (2018).
33. Mleczko, M. J. et al. High current density and low thermal conductivity of atomically thin semimetallic WTe_2. *ACS Nano* **10**, 7507–7514 (2016).
34. Chia, X., Ambrosi, A., Lazar, P., Sofer, Z. & Pumera, M. Electrocatalysis of layered Group 5 metallic transition metal dichalcogenides (MX_2, M = V, Nb, and Ta; X = S, Se, and Te). *J. Mater. Chem. A* **4**, 14241–14253 (2016).
35. Huang, J.-H. et al. Polymorphism control of layered $MoTe_2$ through two-dimensional solid-phase crystallization. *Sci. Rep.* **9**, 8810 (2019).
36. Cui, J. et al. Transport evidence of asymmetric spin–orbit coupling in few-layer superconducting $1T_d$-$MoTe_2$. *Nat. Commun.* **10**, 2044 (2019).
37. Qi, Y. et al. Superconductivity in Weyl semimetal candidate $MoTe_2$. *Nat. Commun.* **7**, 11038 (2016).
38. Chen, F. C. et al. Extremely large magnetoresistance in the type-II Weyl semimetal $MoTe_2$. *Phys. Rev. B* **94**, 235154 (2016).
39. Benalcazar, W. A., Bernevig, B. A. & Hughes, T. L. Quantized electric multipole insulators. *Science* **357**, 61–66 (2017).
40. Kowalczyk, H. et al. Gate and temperature driven phase transitions in few-layer $MoTe_2$. *ACS Nano* **17**, 6708–6718 (2023).
41. Huang, F.-T. et al. Polar and phase domain walls with conducting interfacial states in a Weyl semimetal $MoTe_2$. *Nat. Commun.* **10**, 4211 (2019).
42. Rhodes, D. A. et al. Enhanced superconductivity in monolayer T_d-$MoTe_2$. *Nano Lett.* **21**, 2505–2511 (2021).
43. Tiwari, A. et al. Giant c-axis nonlinear anomalous Hall effect in T_d-$MoTe_2$ and WTe_2. *Nat. Commun.* **12**, 2049 (2021).
44. Zhong, S. et al. Origin of magnetoresistance suppression in thin γ–$MoTe_2$. *Phys. Rev. B* **97**, 241409 (2018).
45. Ma, T. et al. Growth of bilayer $MoTe_2$ single crystals with strong non-linear Hall effect. *Nat. Commun.* **13**, 5465 (2022).

Methods

Materials

Molybdenum (99.9%), tungsten (99.9%), niobium (99%), tantalum (99.8%), titanium (99.9%), vanadium (99.9%), zirconium (99.9%) and tellurium (99.9%) were all obtained from the Tianjin Special Powder Research Institute. Lithium borohydride was obtained from Beijing Innochem Science & Technology Co., Ltd. Polyurethane (99%), ethanol (99%), acetone (99%) and carboxymethyl cellulose (99%) were obtained from Sinopharm Chemical Reagent Co., Ltd. Li_2SO_4 (99.9%), $EMIMBF_4$ (99.9%), acetonitrile (99.9%), polyvinylidene fluoride (99%), Ketjen black (99.9%) and N-methylpyrrolidone (99.9%) were obtained from Shanghai Aladdin Biochemical Technology Co., Ltd. and photoresist AZ4620 from MicroChemicals GmbH. They were all used without further purification.

Preparation of metal tellurides bulk powder

TMT bulk powders MTe_2 (M = Mo, W, Nb, Ta, Ti, Zr, V) were synthesized by the CVT method. In detail, 0.03 mol metal M and 0.06 mol Te powder were ground for 5 min in an agate mortar. The mixture was sealed in an evacuated quartz tube (diameter 1.5 cm, length 20 cm) that was placed in a muffle furnace and directly heated at a rate of 5 °C min^{-1} to 900 °C, at which it remained for 24 h before the furnace was allowed to cool to room temperature. To scale up the synthesis of $NbTe_2$ powder to the hundred-gram scale, four sealed quartz tubes with 0.009 mol metal Nb and 0.18 mol Te powder were used to grow crystals by the CVT method. Because the saturation vapour pressure of tellurides is much lower than that of sulfur, the CVT method enables the simple production of metal tellurides at the hundred-gram scale in the laboratory.

TMT nanosheets by solid lithiation and exfoliation

$LiBH_4$ powder and bulk TMT crystals were mixed in molar ratios (x) of 0.25, 0.5, 0.75 and 1. Because $LiBH_4$ powder is hygroscopic, the mixing process was performed in a glovebox in an argon atmosphere. The mixture was directly heated at 350 °C in a CVD tube furnace with an argon atmosphere for different durations to complete the solid-state lithium intercalation process and form the lithium-ion intercalated TMT compound Li_xMTe_2. The Li_xMTe_2 powder was immediately added to distilled water to form a colloidal solution, which was centrifuged at 3,000 rpm for 5 min to remove unexfoliated bulk crystals. The centrifuged solution was freeze-dried to obtain the TMT nanosheet powder. Note that the freshly prepared Li_xMTe_2 bulk crystal must be used within 12 h to avoid deintercalation. Typically, 0.001 mol $LiBH_4$ powder and 0.001 mol MTe_2 bulk powder were used to prepare the Li_xMTe_2. To scale up the production, more than a hundred grams of Li_xMTe_2 can be prepared by lithium intercalation and exfoliation in a larger CVD furnace.

Preparing MTe_2 nanosheets membranes

Membranes of MTe_2 nanosheets were prepared by vacuum filtrating the colloidal dispersion through a nylon membrane (47 mm diameter, 200 nm pore size). The $Mo_{0.5}W_{0.5}Te_2$/CNT film was prepared by vacuum filtrating a mixed dispersion of $Mo_{0.5}W_{0.5}Te_2$ (16 mg) and CNTs (4 mg).

3D printing of $NbTe_2$ nanosheet scaffolds

First, printable $NbTe_2$ inks were prepared by mixing the $NbTe_2$ nanosheets (1.8 g) with 4 mL of aqueous carboxymethyl cellulose binder (50 M) in a high-speed disperser for 1 h to achieve homogenization. The resulting slurry was used to print on a three-axis micropositioning stage (ZZ-221, ZhongZhi Automation Co., Ltd.) equipped with an air-powered fluid dispenser (JND983A). The $NbTe_2$ inks were extruded through a nozzle with a diameter of 250 μm onto a glass substrate with a printing speed of about 5 mm s^{-1} at a flow rate of 20 psi. After printing, the printed scaffolds with microlattice patterns were freeze-dried for 2 days to remove the solvent.

Screen printing of $NbTe_2$ nanosheet ink

To prepare 2D $NbTe_2$-based screen-printable ink, polyurethane (1 g) was initially dissolved in a dibasic ester solvent (10 mL) to form a transparent solution. Then, 2.5 mL of polyurethane solution was uniformly mixed with the exfoliated $NbTe_2$ nanosheets (1 g) by ball milling to form the screen-printing ink. For the printable 'DICP' logo arrays, a screen mesh (200 mesh) with the predesigned pattern was fixed on the printing table and a non-woven fabric was placed under the screen mesh. Subsequently, the $NbTe_2$-based ink was rapidly screen printed onto the non-woven fabric using a blade. After drying at 60 °C for 12 h, a 2D $NbTe_2$-based ultraflexible pattern was achieved.

Photolithography fabrication of $NbTe_2$ nanosheet-based microelectrodes

The substrates (for example, glass) were cleaned by sequential washing in ethanol and deionized water for 1 h. A thin photoresist (AZ4620) was then coated on the target substrate and exposed to ultraviolet light through a photomask, forming the predesigned pattern of the microelectrodes. $NbTe_2$ nanosheet microelectrodes were then obtained by blade coating with a $NbTe_2$ slurry, followed by lift-off in acetone, assisted by ultrasonic treatment.

Material characterization

The morphology, crystal structure and thickness of the MTe_2 bulk crystals and nanosheets were characterized by SEM (JSM-7900F, JEOL), aberration-corrected TEM (JEM-ARM 300F GRAND ARM, JEOL), AFM (Multi-Mode 3D, Veeco), XRD (SmartLab, Rigaku), XPS (Escalab 250 Xi+, Thermo Fisher) and Raman spectroscopy (LabRAM HR800, HORIBA Jobin Yvon Corporation). The EMI shielding performance of the $Mo_{0.5}W_{0.5}Te_2$/CNT film was characterized by a PAN Network Analyzer (N5222A) in the X-band frequency range (8.2–12.4 GHz).

Device fabrication and transport measurements

For device fabrication and transport measurements, the exfoliated TMT nanosheets were transferred onto SiO_2/Si substrates. After the transfer, samples with different thicknesses were selected by colour contrast under optical microscopy and small markers were deposited near the selected sample for the subsequent nanofabrication process. The electrodes were made by standard electron-beam lithography followed by electron-beam evaporation of bilayer metal Ti/Au (5/90 nm). The thickness of the nanosheets was measured by AFM. Transport measurements were mainly performed in a physical property measurement system. The resistance was measured by an alternating-current method using a standard current-biased low-frequency lock-in technique with an excitation current ranging from 100 nA to 1 μA at a frequency of 17.777 Hz.

Assembly and characterization of lithium–oxygen batteries

The as-prepared catalysts ($NbTe_2$ nanosheets or $NbTe_2$ bulk powder, 80 wt%) with polyvinylidene fluoride (10 wt%) and Ketjen black (EC-600JD, 10 wt%) were ground with several drops of N-methyl pyrrolidone to prepare a slurry and fabricate the cathodes. The battery included an as-fabricated cathode, a glass-fibre separator, 1.0 M lithium bis(trifluoromethanesulfonic)limide in tetraethylene glycol dimethyl ether as the electrolyte and a Li foil anode, which was assembled in an Ar-filled glovebox (H_2O < 0.01 ppm, O_2 < 0.01 ppm). The Li–O_2 batteries were tested as CR2032 button batteries with holes on the cathode side. The cells were tested with a Landt battery testing system (CT3001A). The current density and specific capacity were calculated using the mass of the catalyst. Cyclic voltammetry tests were conducted using a CHI760E electrochemical workstation at a scan rate of 0.1 mV s^{-1} between 2.0 and 4.5 V.

Assembly and characterization of lithium-ion batteries

$Mo_{0.5}W_{0.5}Te_2$ nanosheets and bulk powder electrodes were fabricated by coating an 80-wt% slurry of the active material onto a Cu foil current collector, using a 10-wt% carboxy methyl cellulose sodium binder and 10 wt% Ketjen black (ECP600JD) as the electrical conducting agent and then dried overnight at 100 °C under vacuum. CR2016 coin-type cells were assembled in a glovebox filled with Ar ($H_2O < 0.1$ ppm, $O_2 < 0.1$ ppm), using Li metal as both the counter and reference electrodes, 1 M $LiPF_6$ in ethylene carbonate/dimethylcarbonate/diethyl carbonate (1:1:1 by volume) with 5.0% fluoroethylene carbonate as the electrolyte and Celgard 2500 as the separators. The areal mass loading of electrode was about 1.5–2 mg cm^{-2}. All of the coin cells were evaluated using a Landt CT3002A battery testing system in the constant current mode between 0.1 and 2.5 V (versus Li^+/Li) at 28 °C. Here 1 C is defined as 200 mA g^{-1}.

Assembly and characterization of MSCs

The interdigital microelectrodes of $NbTe_2$-based MSCs were fabricated by vacuum filtration of a dispersion mixture containing $NbTe_2$ (10 mg) and CNTs (2 mg) through an interdigital mask onto a polytetrafluoroethylene membrane. They were then transferred to a polyethylene terephthalate substrate and dried at room temperature. Electrolytes of Li_2SO_4 in distilled water and $EMIMBF_4$ in acetonitrile were coated onto the projected area of microelectrodes. The electrochemical performance was tested on a CHI760E electrochemical workstation.

Data availability

All data supporting the findings of this study are available in the paper and its Supplementary Information. Other raw data are available from the corresponding authors on request. Source data are provided with this paper.

Acknowledgements This work was financially supported by the National Natural Science Foundation of China (grants 22125903, 22209176, 22279137, 12374035, 22075279, E211L5031R and E311L5191R), Basic Science Center Project of the National Natural Science Foundation of China (52188101), the National Key R&D Program of China (grants 2022YFA1504100 and 2023YFB4005204), Innovation Program for Quantum Science and Technology (grant 2021ZD0302600), the China Postdoctoral Science Foundation (2021M703145), International Postdoctoral Exchange Fellowship Program (Talent-Introduction Program) (YJ20210311), the Dalian Innovation Support Plan for High Level Talents (2019RT09), Liaoning Natural Science Foundation (2023-BS-007) and Shanghai Pujiang Talent plan project (23PJ1402000). We thank P. A. Thrower for carefully reviewing and revising the manuscript.

Author contributions Z.-S.W., N.K. and H.-M.C. conceived and supervised the project. L.Z. conducted the production and characterization of the TMT nanosheets. Z.Y., Y.F., S.F. and D.-M.S. carried out transport measurements of the TMT nanosheet devices. Q.J. performed the XRD and XPS of the alloyed nanosheets. Y.D. characterized the Li–O_2 batteries. P.D. tested the electrochemical performance of the MSCs. Z.B. characterized the lithium batteries. J.Ma., J.Mi, S.W., Z.G. and S.Z. carried out the 3D printing, photolithography and screen printing of the $NbTe_2$ nanosheet ink. H.Z. characterized the EMI shielding performance of the $Mo_{0.5}W_{0.5}Te_2$/CNT film. M.L. obtained the spherical aberration-corrected TEM images. L.Z., Z.Y., P.D., N.K., Z.-S.W. and H.-M.C. wrote the manuscript. All authors contributed to discussions.

Competing interests The authors declare no competing interests.

Additional information
Supplementary information The online version contains supplementary material available at https://doi.org/10.1038/s41586-024-07209-2.
Correspondence and requests for materials should be addressed to Ning Kang, Zhong-Shuai Wu or Hui-Ming Cheng.
Peer review information *Nature* thanks Zheng Liu, Kian Ping Loh and the other, anonymous, reviewer(s) for their contribution to the peer review of this work.

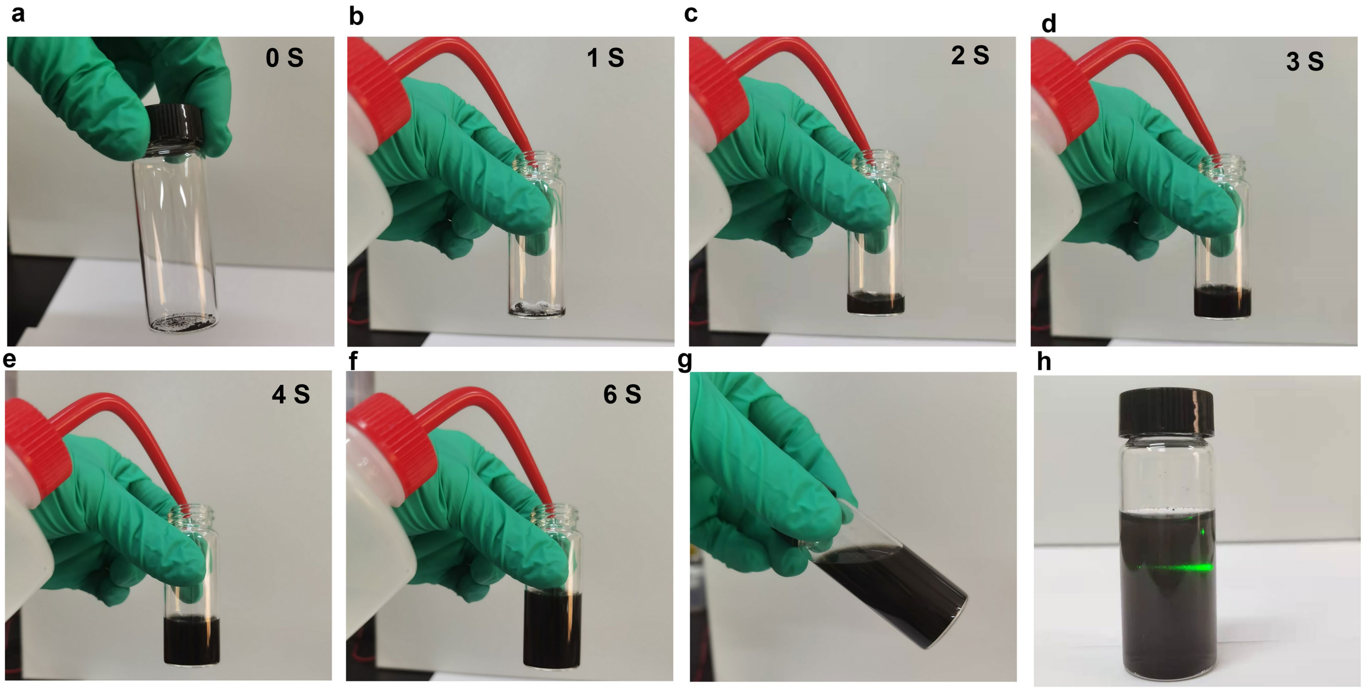

Extended Data Fig. 1 | Illustration of the hydrolysis process of lithiated $NbTe_2$ bulk powder into a nanosheet colloid solution. **a**–**g**, Photographs of the exfoliation process of Li_1NbTe_2 by adding distille water to the glass bottles at different times. Li_1NbTe_2 is hydrolysed into $NbTe_2$ nanosheets by the generation of H_2 gas, resulting in a homogenous colloidal dispersion. **h**, Tyndall effect of a $NbTe_2$ nanosheet colloid solution.

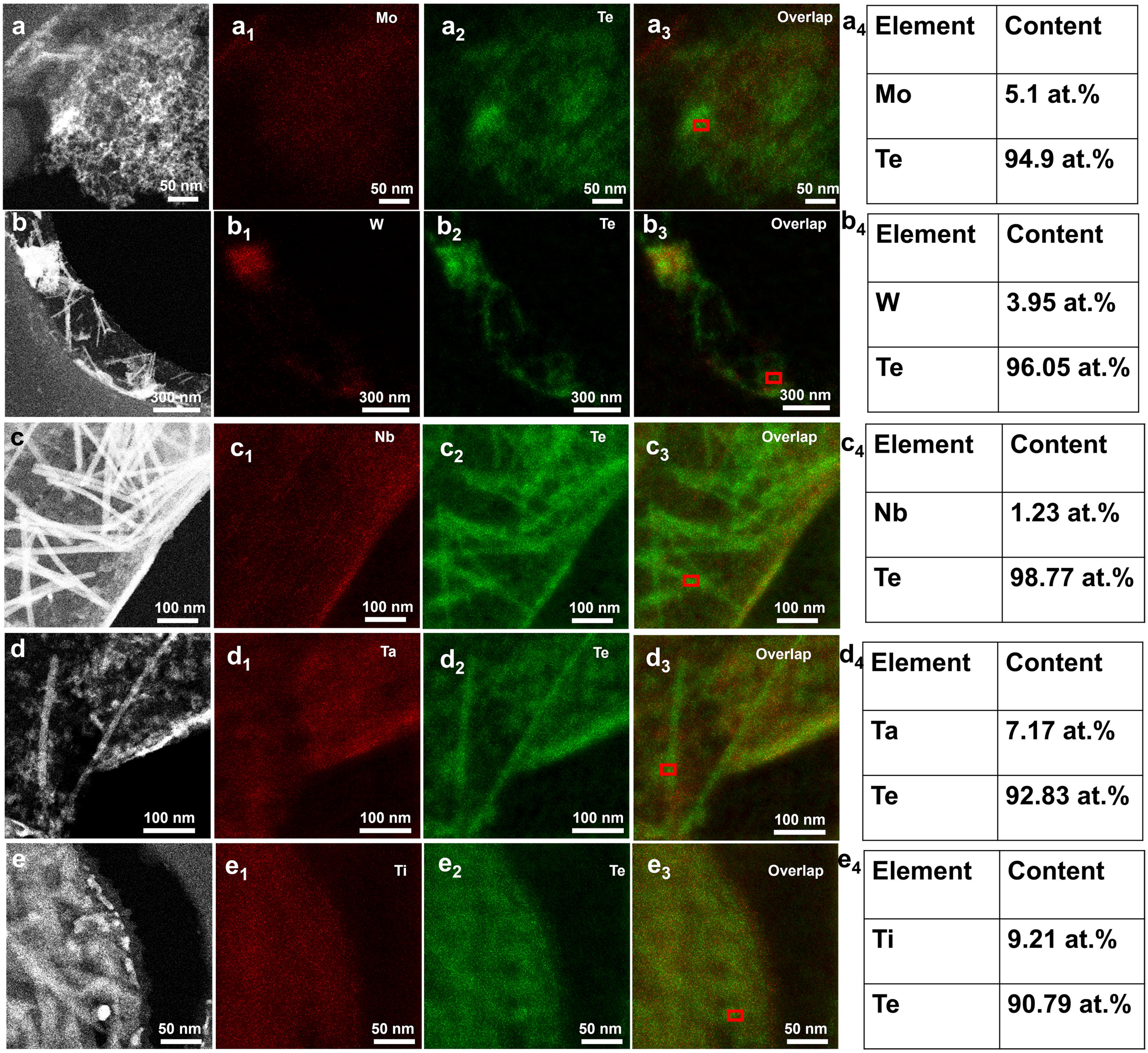

a_4

Element	Content
Mo	5.1 at.%
Te	94.9 at.%

b_4

Element	Content
W	3.95 at.%
Te	96.05 at.%

c_4

Element	Content
Nb	1.23 at.%
Te	98.77 at.%

d_4

Element	Content
Ta	7.17 at.%
Te	92.83 at.%

e_4

Element	Content
Ti	9.21 at.%
Te	90.79 at.%

Extended Data Fig. 2 | Morphology and elemental characterization of various TMT nanosheets using a long lithium intercalation time when the molar ratio of $LiBH_4$ to MTe_2 is equal to 1. a–a₄, $MoTe_2$ nanosheets after lithium intercalation for 24 h. **a**, HAADF-STEM image. EDS elemental maps of Mo (**a_1**), Te (**a_2**) and mixed Mo and Te (**a_3**). **a_4**, Table of the elemental content of the marked area in **a_3**. **b–b_4**, WTe_2 nanosheets after lithium intercalation for 6 h. **b**, HAADF-STEM image. EDS elemental maps of W (**b_1**), Te (**b_2**) and mixed W and Te (**b_3**). **b_4**, Table of the elemental content of the marked area in **b_3**. **c–c_4**, $NbTe_2$ nanosheets after lithium intercalation for 24 h. **c**, HAADF-STEM image. EDS elemental maps of Nb (**c_1**), Te (**c_2**) and mixed Nb and Te (**c_3**). **c_4**, Table of the elemental content of the marked area in **c_3**. **d–d_4**, $TaTe_2$ nanosheets after lithium intercalation for 6 h. **d**, HAADF-STEM image. EDS elemental maps of Ta (**d_1**), Te (**d_2**) and mixed Ta and Te (**d_3**). **d_4**, Table of the elemental content of the marked area in **d_3**. **e–e_4**, $TiTe_2$ nanosheets after lithium intercalation for 6 h. **e**, HAADF-STEM image, EDS elemental maps of Ti (**e_1**), Te (**e_2**) and mixed Ti and Te (**e_3**). **e_4**, Table of the elemental content of the marked area in **e_3**. The HAADF-STEM EDS elemental maps show that the morphology of the decomposition products is a nanobelt and that Te is present in all samples after a long lithium intercalation time.

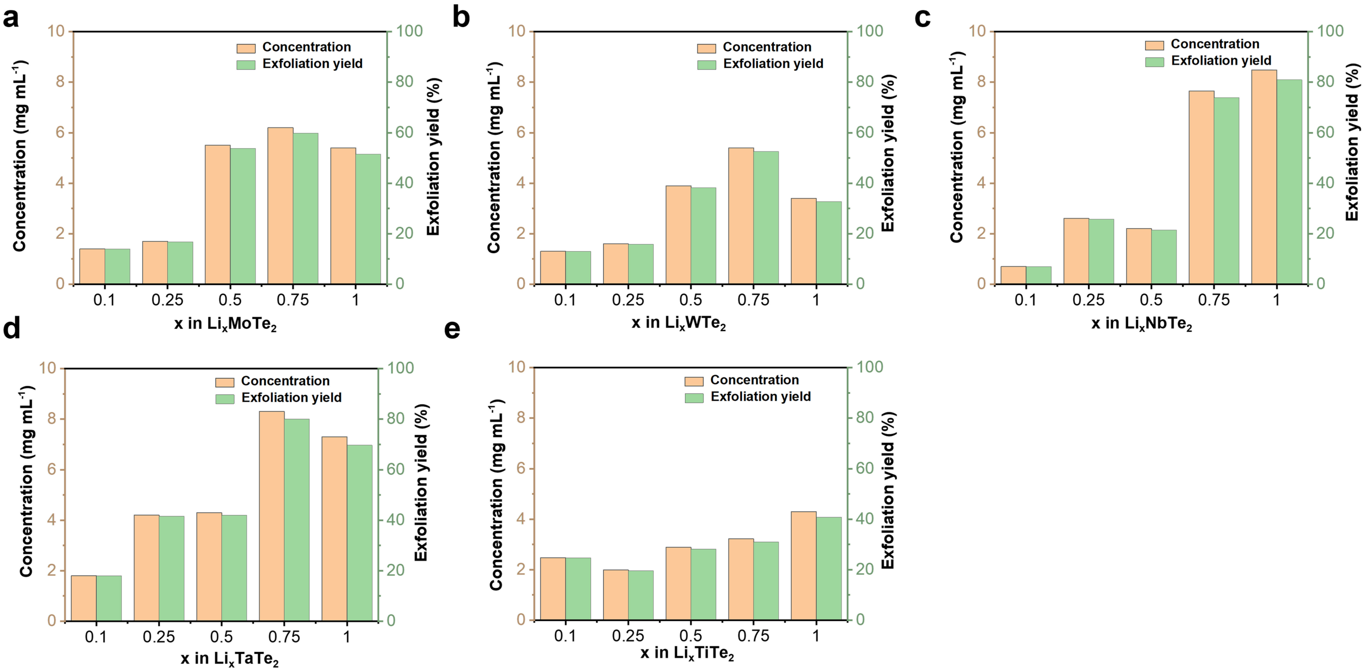

Extended Data Fig. 3 | The influence of LiBH$_4$ content on exfoliation yield and solution concentration. **a**, MoTe$_2$ nanosheets. **b**, WTe$_2$ nanosheets. **c**, NbTe$_2$ nanosheets. **d**, TaTe$_2$ nanosheets. **e**, TiTe$_2$ nanosheets. We found that molar ratios of LiBH$_4$ to MTe$_2$ ranging from 0.75 to 1 are suitable for achieving a high exfoliation yield of more than 60% for MoTe$_2$, 50% for WTe$_2$, 80% for NbTe$_2$, 80% for TaTe$_2$ and 40% for TiTe$_2$.

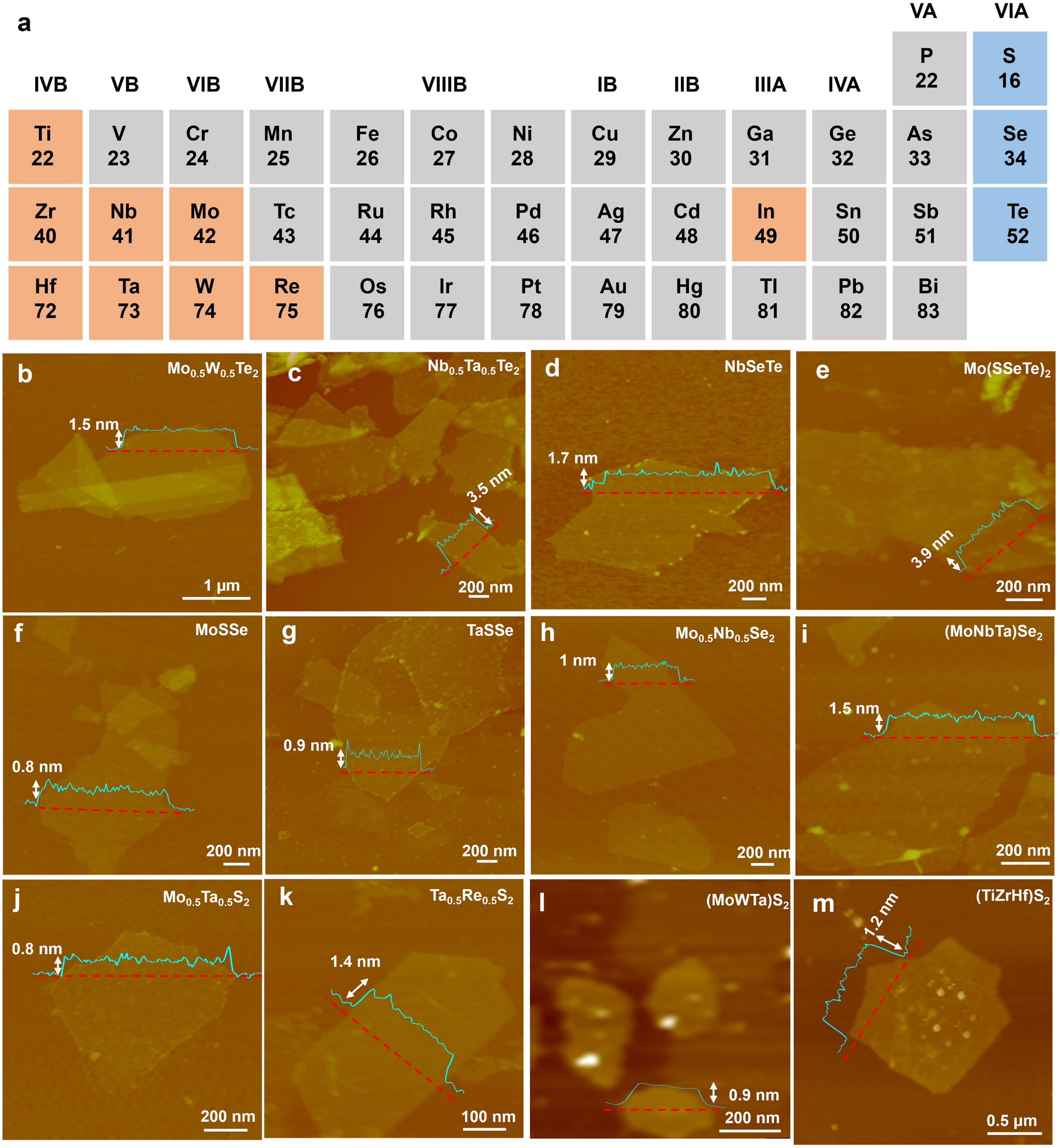

Extended Data Fig. 4 | Summary of synthesizable materials using solid lithiation and exfoliation. a, Periodic table showing the metals (highlighted in brown) and chalcogens (highlighted in blue) that have the possibility of forming layered sulfides, selenides and tellurides. **b**–**m**, AFM images and height profiles (insets) of 12 types of telluride, selenide and sulfide nanosheet. **b**, $Mo_{0.5}W_{0.5}Te_2$. **c**, $Nb_{0.5}Ta_{0.5}Te_2$. **d**, NbSeTe. **e**, $Mo(SSeTe)_2$. **f**, MoSSe. **g**, TaSSe. **h**, $Mo_{0.5}Nb_{0.5}Se_2$. **i**, $(MoNbTa)Se_2$. **j**, $Mo_{0.5}Ta_{0.5}S_2$. **k**, $Ta_{0.5}Re_{0.5}S_2$. **l**, $(MoWTa)S_2$. **m**, $(TiZrHf)S_2$.

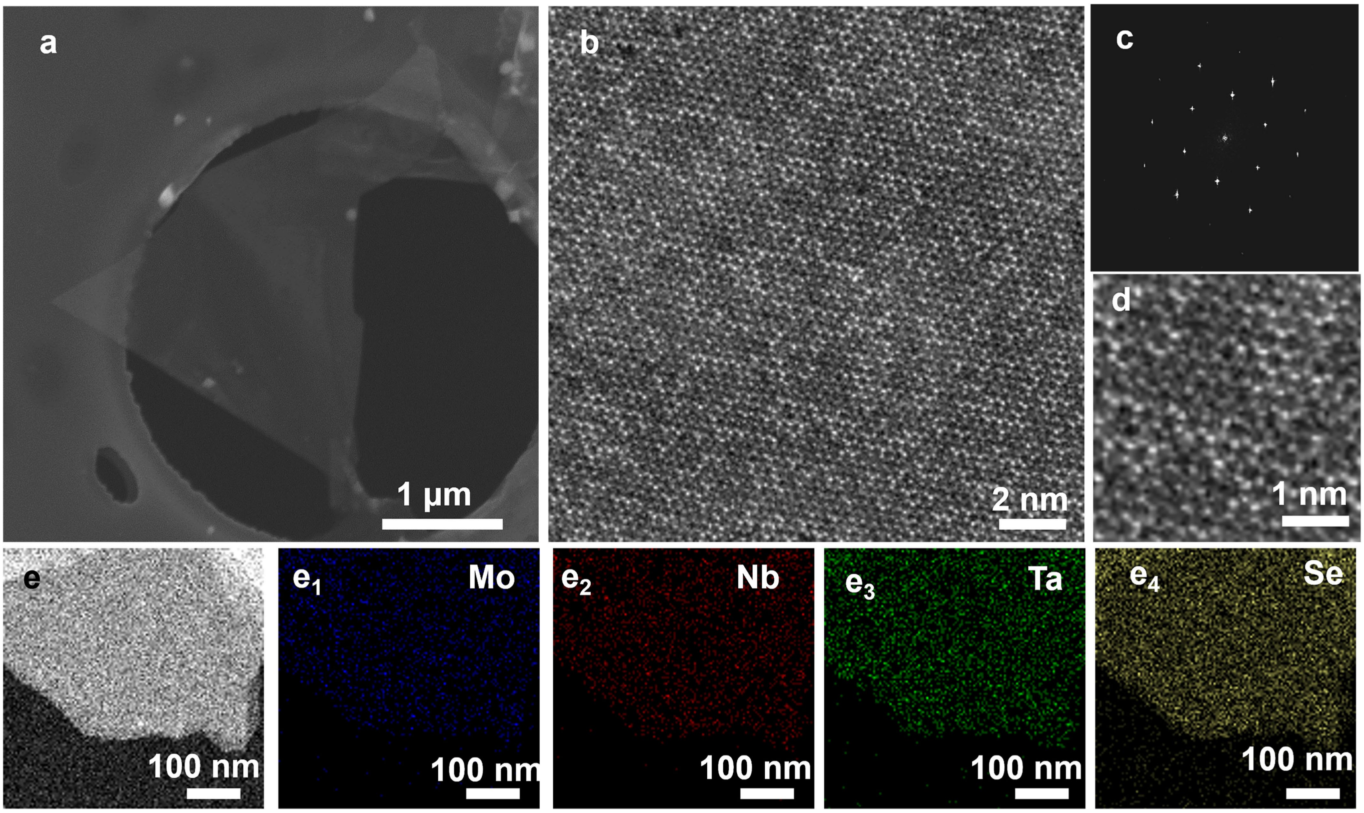

Extended Data Fig. 5 | Structural characterizations of a (MoNbTa)Se_2 nanosheet. a, Low-magnification STEM image. **b**, Atomic-resolution HAADF-STEM image. **c**, FFT pattern. **d**, Magnified HAADF-STEM image of **b**. **e**–**e$_4$**, HAADF-STEM image and EDS elemental maps of Mo, Nb, Ta and Se.

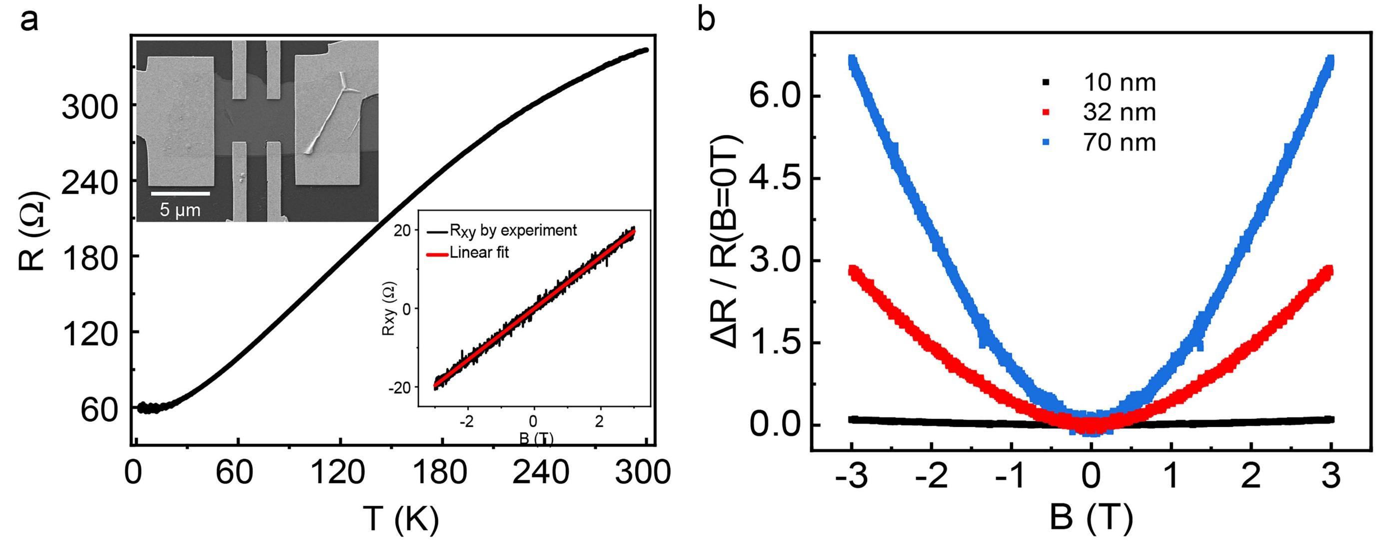

Extended Data Fig. 6 | Transport properties of a $Mo_{0.5}W_{0.5}Te_2$ nanosheet. **a**, Low-temperature transport measurement of a $Mo_{0.5}W_{0.5}Te_2$ thin nanosheet. The temperature dependence of resistance shows metallic behaviour. Upper inset, SEM image of a fabricated device with multiterminal Hall-bar geometry. Lower inset, the Hall measurement shows a carrier density of 9.6×10^{13} cm^{-2}. **b**, Magnetoresistance, defined as $(R(B) - R(B = 0))/R(B = 0)$, plotted as a function of magnetic field for $Mo_{0.5}W_{0.5}Te_2$ thin films with thicknesses ranging from 10 to 70 nm. It is seen that the positive magnetoresistance is substantially decreased with decreasing thickness.